Regulation of oriented NO photooxidation to circumvent NO_2 with high-coordinated M–N_5 (M = Fe, Co, Mn, Ti) sites and far–carbon defects

Zhao Hu [a],[1], Yujiao Zhang [a],[1], Yan Wang [b], Jinshu Huang [a], Song Yang [a], Hu Li [a],*

[a] *National Key Laboratory of Green Pesticide, Key Laboratory of Green Pesticide & Agricultural Bioengineering, Ministry of Education, State-Local Joint Laboratory for Comprehensive Utilization of Biomass, Center for R&D of Fine Chemicals, Guizhou University, Guiyang, Guizhou 550025, China*
[b] *Hunan Provincial Key Laboratory of Micro & Nano Materials Interface Science, College of Chemistry and Chemical Engineering, Central South University, Changsha, Hunan 410083, China*

A B S T R A C T

The targeted oxidization of trace NO to NO_3^- instead of toxic NO_2 *via* photocatalytic process represents one of the promising protocols for assuring environmental benefits. A novel type of graphite carbon nitride (CN) photo-catalysts with high coordination sites (M–N_5; M = Fe, Co, Mn, Ti) and far–carbon defects were manufactured by reconstructing the low coordination structure (M–N_4). The mingled characterizations and theoretical calculations demonstrated that the reconstructed sites could improve the charge and energy transfer process of the exciton to precisely regulate the activation process of O_2, while inhibiting the activation of adsorbed H_2O. Superior orientation to form superoxide radical and singlet oxygen, rather than hydroxyl radical, showed excellent NO removal rates (68.6%) and superior NO_3^- selectivity (about 100%) under visible–light irradiation. This work proposes a unique mechanism via tailored construction of highly coordinated structures for selective NO oxidation to achieve the goal of atmospheric purification.

1. Introduction

In the various techniques for efficient removal of atmospheric pol-lutants, photocatalytic selective oxidation of trace NO to non-toxic and harmless NO_3^- in the gas phase is rifely considered to be a model case of direct use of solar energy in chemical energy, because solar energy is the most abundant energy [1,2]. Graphite carbon nitride (CN) is an important photocatalyst [3–5], but it provides low NO removal effi-ciency mainly due to its rapid recombination of photogenerated charge carriers and unsatisfactory energy transfer of excitons, so that it cannot produce the necessary reactive oxygen species (ROSs) [6–8]. Impor-tantly, in the past, CN–based photocatalysts reported exhibited subop-timal NO_3^- selectivity, especially the emission of the toxic by–product NO_2 at 20–100 ppb [9–11], which is mainly caused by the existence of multiple pathways during the conversion of odd–electron NO molecules in the aerobic system [12]. Therefore, it is expected to improve the ac-tivity of CN and expand its application in the air purification field.

Among the many modification strategies of CN, single atom anchoring not only enhances the utilization of atoms, but increases the surface energy of the catalyst as well, realizing the fast activation of the reactant or O_2 molecules [7,13,14]. As we know, the coordination structures of the single atom are able to influence the course of catalytic reactions [15–18], especially the activation of O_2 molecules for aerobic reactions [17]. Nevertheless, the structure–activity relationship be-tween the coordination number of the active site and the activation of O_2 molecular *via* energy transfer and charge transfer are still unclear. Generally, the modification of low–coordinated single atomic sites (M–N_x, x≤4) has been shown to greatly enhance the separation of photoexcited charge carriers of CN [19–21]. However, the construction of these special atomic sites usually results in insufficient generation of superoxide radicals (•O_2^-) and rapid conversion of •O_2^- to hydroxyl radicals (•OH), thus unable to achieve the target conversion of NO to NO_3^- [22,23]. Alternatively, the introduction of carbon defects can also extend the visible light response range of CN, but the performance of activated O_2 molecular is unattractive, so the photocatalytic activity is not brilliant [3,24]. As expected, for CN, the construction of carbon vacancies can also regulate the coordination number to form the M–N_4 (e.g., M = Fe) structure, which is accessible to quickly activate O_2, thus accomplishing ascendant catalytic performance [21]. Among the developed protocols, the modulation of M–N_4 active centers with a

* Corresponding author.
  E-mail address: hli13@gzu.edu.cn (H. Li).
[1] The authors contribute equally to this work.

relatively low coordination number facilitates the charge migration ability [19,20], thereby activating the ground state $^3O_2$ to $\bullet O_2^-$. By regulating the rapid formation of $\bullet O_2^-$ on the catalyst surface, the NO conversion rate reached 63.0%, and the corresponding product NO_3^- selectivity could be more than 90.0% [25]. In other words, the reasonable construction of carbon defects and $M–N_x$ sites can be expected to enhance photocatalytic performance. Recently, highly coordinated atomic active centers ($M–N_5$) have also attracted more attention because they can promote the separation of photogenerated charge carriers and the energy transformation of singlet excitons [26,27]. For the activation of O_2 molecular, the efficient energy transfer of excitons leads to the direct activation of the $^3O_2$, and then forms the extremely significant ROSs, singlet oxygen ($^1O_2$) [28,29]. In fact, long–lived $^1O_2$ also plays a very remarkable role in the process of NO oxidation, thus increasing the removal rate of NO and the selectivity of NO_3^- [12,30]. For example, when the photocatalyst generates abundant $^1O_2$, the corresponding selectivity of NO_3^- can approach 90.1% [30]. Unfortunately, in previous studies, for CN, the formed $^1O_2$ was determined due to the charge transfer process, that is, the interaction of $\bullet O_2^-$ and photoexcited holes, and the formation of $^1O_2$ was often ignored through the energy transfer of carrier. In this context, a novel single–site modified CN material can be precisely designed to enhance the charge transfer and energy transfer process of photoexcited charge carriers, obtaining high content of main ROSs (O_2^- and $^1O_2$) to optimize the selectivity of the end products in the aerobic oxidation. Inspired by this, a simple and inexpensive strategy to precisely modulate a high–coordinated $M-N_x$ ($x > 4$) structure with specific defects on the CN surface may realize photocatalytic NO oxidation of high selectivity.

In this work, a series of far carbon defects–modified CN photocatalysts with high-coordinated $M–N_5$ sites were prepared by the thermal treatment and illustrated to show excellent activity for the conversion of NO to NO_3^- along with extremely low NO_2 production under visible light in an aerobic atmosphere. The elaborately constructed $M-N_5$ sites and far carbon defects with the charge transfer and energy transfer capacity enabled the formation of much-needed reactive oxygen species. Meanwhile, the relationship between the coordination number, the evolution of ROSs to generate $\bullet O_2^-$ and $^1O_2$, and the photocatalytic performance were also systematically investigated and expounded. Furthermore, the developed synthesis strategy also exhibited strong universality to prepare a wide range of photocatalysts comprising different precursors or metals with pronounced performance in directional oxidation of NO to NO_3^-.

2. Experiment section

2.1. Preparation of CNF_x photocatalysts

Yellow CN was first obtained by heating 10 g of melamine in a 100 mL ceramic crucible with a cover at 550 °C for 4 h. Then, 50 mg of cyclopentadienyliron dicarbonyl dimer (CDD) was evenly dispersed in 500 mL DMF with ultrasound for 30 min, and 500 mg of CN was added and stirred for 12 h to achieve saturation adsorption. After methanol washing and drying, the resulting reddish-brown solid was transferred to a tube furnace, and treated at 350 °C for 4 h under an H_2/Ar (10%, v/v) atmosphere, resulting in the target photocatalyst denoted as CNF_5. When the amount of CDD was 10, 20, 100, and 200 mg, the corresponding samples were named CNF_1, CNF_2, CNF_{10}, and CNF_{200}, respectively. For comparison, CN was treated under the same conditions without CDD.

2.2. Preparation of CNF_5T_y photocatalysts

In a typical procedure, 0.5 g of the above-prepared CNF_5 sample was put into a tube furnace with a heating rate of 1 °C/min at 550 °C for 4 h under an N_2 atmosphere, followed by calcination again under the same conditions, resulting in the crimson sample, which was designated as

CNF_5T_2. The "y" label represents the calcination times under an N_2 atmosphere, where the obtained samples calcined once and 3 times were labeled as CNF_5T_1 and CNF_5T_3, respectively. Note that to expand the generalizability of the synthesis strategy, melamine was replaced with cyanamide, dicyandiamide, urea, and thiourea, and the resulting samples were labeled CA–Fe, DA–Fe, UR–Fe, and TU–Fe, respectively. In an identical procedure except that CDD was replaced with dicarbonylcyclopentadienyl cobalt, cyclopentadienylmanganese tricarbonyl, and bis(cyclopentadienyl)dicarbonyl titanium, and the obtained samples were denoted as CN–Co, CN–Mn, and CN–Ti, respectively.

In addition, the details of catalyst characterization, catalytic activity, DFT theoretical calculations, and other relevant tests are presented in the Supporting Information.

3. Results and discussion

3.1. Crystal phase and structure

CN functionalized with atomic $Fe–N_5$ sites and carbon vacancies (abbreviated as CNF_5T_y, where y denotes the number of calcination under an N_2 atmosphere), were prepared using a simple two-step method (Fig. 1A). Firstly, CDD was adsorbed on the CN surface, followed by *in situ* calcination under a reducing atmosphere to form $Fe–N_4$ sites anchored on CN (CNF_x, x denotes the added amount of CDD). Then, CNF_5T_y catalysts with $Fe–N_5$ sites and far carbon vacancies (Cv) were successfully prepared by calcining optimized CNF_5 directly under an N_2 atmosphere. As shown in Fig. 1B, only two X-ray diffraction (XRD) peaks at 2θ of 13.0 ° and 27.3 ° were observed for all samples, matching with (100) and (002) lattice planes of CN [13], respectively. The characteristic diffraction peaks gradually decreased with increasing the Fe content and calcination times under N_2, which might be the interaction between Fe atoms and layers of CN, thus causing the plane structure to be damaged. Importantly, no peaks of Fe species and CDD were also observed in Fig. 1B, suggesting that the pyrolyzation of CDD could *in situ* produce highly dispersed Fe atoms on the CN surface. Furthermore, the C–N bond and heptazine ring unit vibration peaks of CN at 1200–1700 cm^{-1} and 809 cm^{-1} could be seen in Fig. 1C [7], respectively, and no obvious vibration peaks of CDD and Fe–O bond were found in CN, CNF_5, and CNF_5T_2 samples, matching with XRD results. It should be noted the intensity of the –OH vibration peak at 3179 cm^{-1} in CNF_5T_2 was significantly weaker than that in CN and CNF_5 [31], implying the strongest activation of adsorbed water on the CNF_5T_2 surface. Transmission electron microscopy (TEM) images showed CN of a multi–layer structure (Fig. S1). When the mixture of melamine adsorbed by CDD was used as the precursor, the obtained CNF_5 was also composed of multilayer nanosheets. Importantly, by *in situ* stripping CNF_5 in the heat under N_2, the layers of CNF_5T_2 were thinner (Fig. S1), as illustrated by SEM (Fig. S2). Moreover, atomic dispersed Fe atoms (Fig. 1D and E, white spots in yellow circles) were discovered in the high-angle angular dark field-scanning transmission electron microscopy (HADDF–STEM) images of the CNF_5 and CNF_5T_2 samples, and elemental mappings also demonstrated that Fe atoms were uniformly dispersed in the framework of CN (Fig. 1F). It meant that the anaerobic calcination had no effect on the atomic dispersion of Fe atoms.

To explore the fine structure of single Fe atoms in these catalysts, the X-ray absorption near–edge structure (XANES) and the corresponding extended X-ray absorption fine structure (EXAFS) spectra were measured. The chemical valences of Fe atoms in CNF_5 and CNF_5T_2 were identified between +2 to +3 (Fig. 2A). Moreover, compared to CNF_5, the absorption Fe K-edge energy for CNF_5T_2 was assigned higher, indicating that Fe atoms in CNF_5T_2 got a higher oxidation state or coordination number (Fig. 2A and inset). In the EXAFS spectra of CNF_5 and CNF_5T_2, no apparent Fe–Fe bonds were observed (Fig. 2B), suggesting that Fe species were present on the CNF_5 or CNF_5T_2 surface as single atoms, which was consistent with the results of HADDF–STEM. Additionally, the Fe–ligand peaks of CNF_5 and CNF_5T_2 were ascribed to the
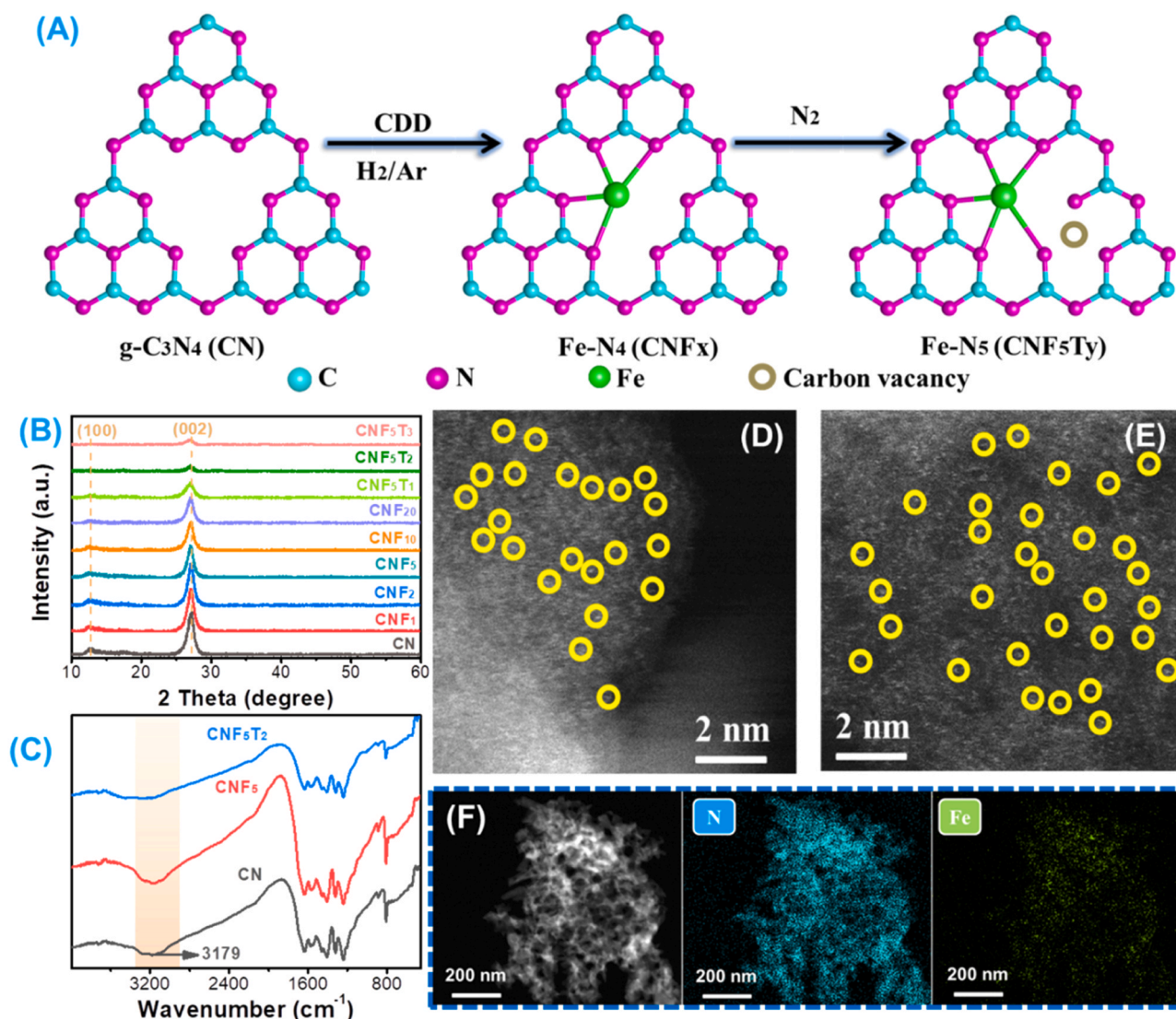
Fig. 1. Schematic illustration of preparing CNF_5T_y samples (A). XRD patterns (B) and FT-IR spectra (C) of *as*-prepared samples. HADDF-STEM images of CNF_5 (D) and CNF_5T_2 (E). Elemental mappings of CNF_5T_2 (F).

coordination of Fe–N bonds. The Fe–N bond length of CNF_5T_2 was longer than that of CNF_5 in the first shell (Fig. 2B), which might be due to the higher coordination number of Fe–N in CNF_5T_2. The quantitative parameters of the Fe–N sites were further obtained using least-squares EXAFS curve fitting (Fig. S3), and the corresponding fitting results are listed in Table S1. The average coordination numbers of Fe–N bonds in CNF_5 and CNF_5T_2 were determined to be 4.1 ± 1.0 and 4.8 ± 1.5, respectively (Table S1). The wavelet transforms (WT) of CNF_5 and CNF_5T_2 only proved intensity maxima at ca. 4.0 Å^{-1} and ca. 4.3 Å^{-1}, respectively (Fig. 2C and D). These further confirmed that the CNF_5T_2 sample with a Fe–N coordination number of 5 (Fe–N_5) could be successfully prepared by calcining the CNF_5 sample with a coordination number of 4 (Fe–N_4). The content of Fe in CNF_5T_2 was obtained to be 0.96 wt% using inductively coupled plasma optical emission spectrometer (ICP–OES) (Table S2).

Apparently, the formation of the Fe–N structure with a high coordination number induced by simple thermal treatment needed to be further investigated. According to the X-ray photoelectron spectroscopy (XPS) survey scan, the inclusion of only C, N, and O elements in CNF_5 and CNF_5T_2, without obvious Fe elements (Fig. S4A), might be the reason for the low amount of introduced Fe. Of the three samples (CN, CNF_5, and CNF_5T_2), only three fitting C 1 s XPS peaks (Fig. S4B) were

noted to be 288.0 eV (N–C═N), 286.2 eV (C–NH_x), and 284.6 eV (C–C, carbon impurity), respectively [4]. More importantly, the two peak area ratios (1: N–C═N and 2: C–C) of CNF_5T_2 ($S_{1/2} = 1.7$) were smaller than those of CN ($S_{1/2} = 2.9$) and CNF_5 ($S_{1/2} = 3.0$) in Fig. S4B, demonstrating the formation of Cv at N–C═N sites in CNF_5T_2 [3]. The N 1 s XPS peaks of these samples were also fitted to form three peaks (Fig. S4C), which were 400.9 (–NH_2), 399.6 (N–C_3), and 398.6 eV (C–N═C), respectively [32,33]. Meanwhile, in the Fe 2p XPS spectra, the two weak peaks (725.1 and 711.7 eV) were attributed to $2p_{1/2}$ and $2p_{3/2}$ of Fe^{3+}, respectively, and the two strong peaks at 723.3 and 709.5 eV were assigned to $2p_{1/2}$ and $2p_{3/2}$ of Fe^{2+}, respectively (Fig. S4D) [34]. The remaining Fe 2p peaks tended to be other Fe oxidizing species (Fig. S4D) [34]. Also, the grafting of the strongly distorted Fe–N_4 sites to the CN surface increased the number of unpaired electrons of odd carbon atoms in the aromatic ring of CN, thus generating a stronger single electron spin resonance (EPR) for CNF_5 (Fig. S5). Instead, the EPR intensity of CNF_5T_2 decreased because the formation of Cv in CN inhibited the localization of the π-conjugated structure, resulting in a decrease in the number of single electrons [24]. These discussions further elucidated that CNF_5 samples with low-coordination (Fe–N_4) calcined under N_2 might induce the formation of high–coordination structures (Fe–N_5) accompanied by Cv. It was necessary
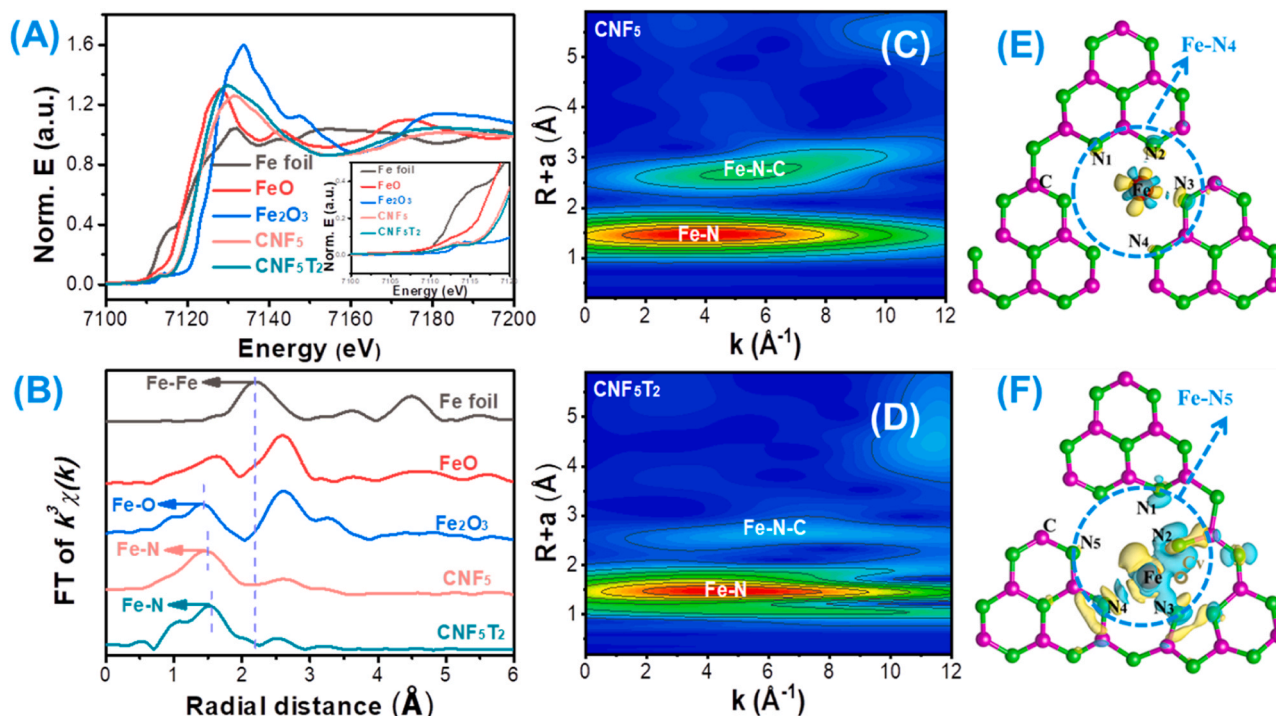
Fig. 2. Fe K-edge XANES spectra (A). Fourier transform spectra of different Fe-containing samples (B). Wavelet transform of CNF_5 (C) and CNF_5T_2 (D) samples. Optimized structures of CNF_5 (E) and CNF_5T_2 (F).

to deeply resolve the spatial relationship between Cv and Fe–N_5 sites, due to many possible positions of Cv in the six-fold cavity of CN. Accordingly, five possible sites of Cv on the surface of CN were investigated using theoretical calculations (Fig. S6A). From a thermodynamic perspective, the formation energy of Cv at the "5" position (–2.02 eV) was greatest in comparison with other positions (Fig. S6B). The corresponding optimized structures of each site were summarized in Fig. S6C. The existence of only "5" sites for Cv was reasonable since none of the remaining sites corresponded to the structures with a coordination number of 5 (Fig. S6C), thus Cv on the "5" site was defined as far Cv.

According to the above optimization, the possible structures of CNF_5 and CNF_5T_2 were demonstrated in Fig. 2E and F, respectively.

3.2. Charge transfer and energy transfer processes

As expected, the CNF_5T_2 samples gave evidence of greater visible light capture efficiency compared to CN and CNF_5, according to the measured light–trapping performance (Fig. 3A) and the calculated light absorption capacity (Fig. S7). The reason for this phenomenon was the construction of Fe–N_5 sites and far Cv, which caused the CN surface to be
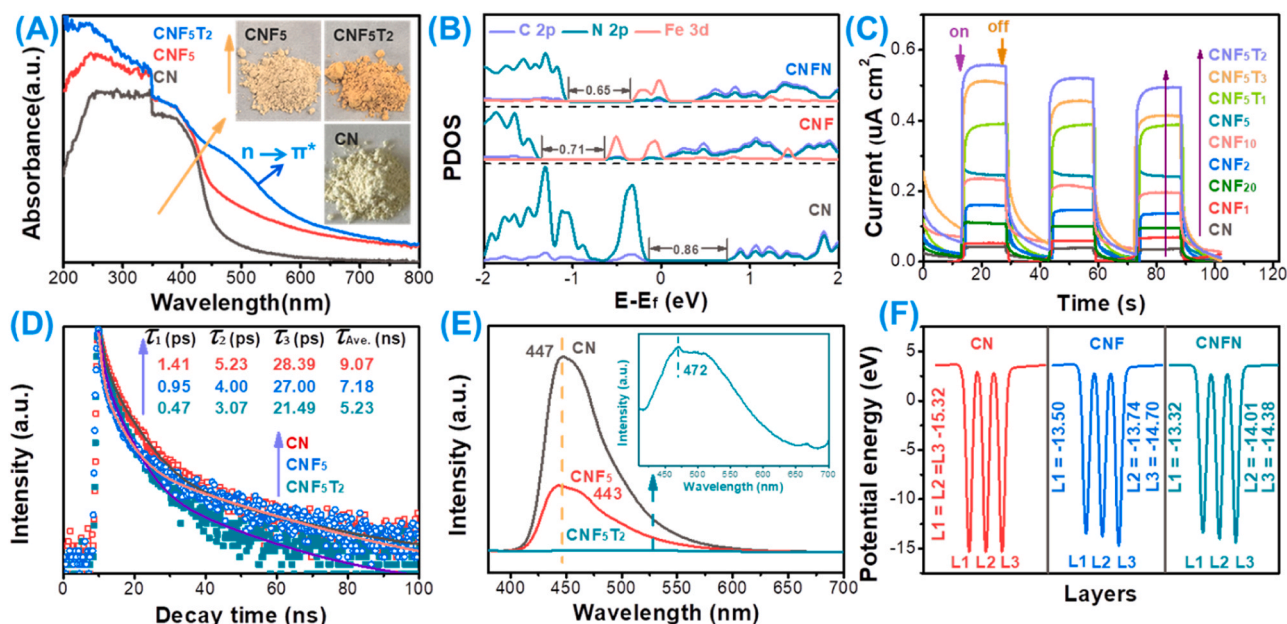

Fig. 3. Diffused reflectance spectra (A) and sample images (inset), density of states (B), photocurrent (C), TRFDS (D), PL (E), and the calculated electrostatic potential (F).

strongly distorted and the planar structure to be destroyed. Moreover, the forbidden transition from n to π* in CN was broken, which made the trapping range of visible light red-shifted [35]. It was also verified again by the change in the color of the catalyst from yellow to faint red, and then to crimson (Fig. 3A, inset). In addition, the calculated band gap decreased from 0.86 eV for CN to 0.71 eV for CNF and then to 0.65 eV for CNFN, and the conduction band (CB) for CNF and CNFN was mainly composed of impurity states of Fe 3d and N 2p (Fig. 3B). However, the potential at the conduction band bottom of CNFN was more negative than that of CNF (Fig. 3B), indicating that the introduced Fe–N_5 sites and far Cv expanded the visible light absorption range and promoted carrier separation. Meanwhile, the photocurrent of all samples (CNF_5T_y) was higher than those of CN and CNF_x under illumination (Fig. 3C), especially for the CNF_5T_2 with the maximum current at approximately 0.56 µA cm^{-1}. With the increase of the calcination times to 3, the photocurrent intensity of CNF_5T_3 decreased to about 0.44 µA cm^{-1}, which was caused by excessive damage to the crystal structure (Fig. 3C). The radius corresponding to all samples in the Nyquist plots was also endowed with a homologous tendency (Fig. S8). According to time-resolved fluorescence decay spectroscopy (TRFDS) in Fig. 3D, the average lifetime and the lifetime of positive components of the CNF_5T_2 sample were more delayed than those of CN and CNF_5, signifying that the long-lived carriers of CNF_5T_2 facilitated the increase in transition rate of the electron from the ground state to the excited state [36], thus extending the lifetime of the excited electrons to improve the catalyst performance. As displayed in Fig. 3E, the photoluminescence (PL) intensity of CNF_5T_2 was also lower than that of CN and CNF_5, suggesting that the radiative recombination of the carriers was more restricted [32]. The electrostatic

potential at the first layer (L1) of CN, CNF, and CNFN was calculated to be 15.32, 13.50, and 13.32 eV, respectively (Fig. 3F). It was suggested that when Fe–N_5 structures and far Cv were grafted onto the CN surface, electrons could be migrated more easily from the bulk to the surface in photocatalytic reactions. The Bader effective charge (Δq) of the nitrogen atoms around Fe atoms in CNFN was calculated to be more negative in the comparison with CN and CNF (Fig. S9), which matched with the electrostatic potential of L1 (Fig. 3F). These results insinuated that the introduced Fe–N_5 structures with high coordination numbers and far Cv enhanced the rapid transfer of photoexcited charges.

It is known that the photocatalyst activity was influenced by both the charge transfer process and the energy transfer process [37]. Given this, we further investigated the photoelectric properties of the catalyst. In comparison with CN and CNF_5, the fluorescence emission peak of CNF_5T_2 was red-shifted to 472 nm (Fig. 3E, inset), meaning that for CNF_5T_2 after excitation, excited electrons transition to high energy levels were more conducive to spontaneous radiation and release energy through the strategy of energy transfer [38]. Remarkably, the lifetime of triplet excitons over CNF_5T_2 (23.7 µs) was longer than that of CN (4.9 µs) and CNF_5 (11.6 µs) under Ar atmosphere (Fig. 4A–C), benefiting to improve the interfacial energy transfer, which was used to activate molecular O_2 over CNF_5T_2 for generating $^1O_2$ with superior oxidation [39]. As one would expect, the triplet state lifetime of these three samples (especially CNF_5T_2) was drastically reduced in the O_2 atmosphere (Fig. 4D–F), illustrating efficient energy transfer from the catalyst surface to adsorbed oxygen. Although CN was regarded as a typical material with a weak exciton effect, its exciton effect should not be ignored [40]. In temperature-dependent photoluminescence spectra, the
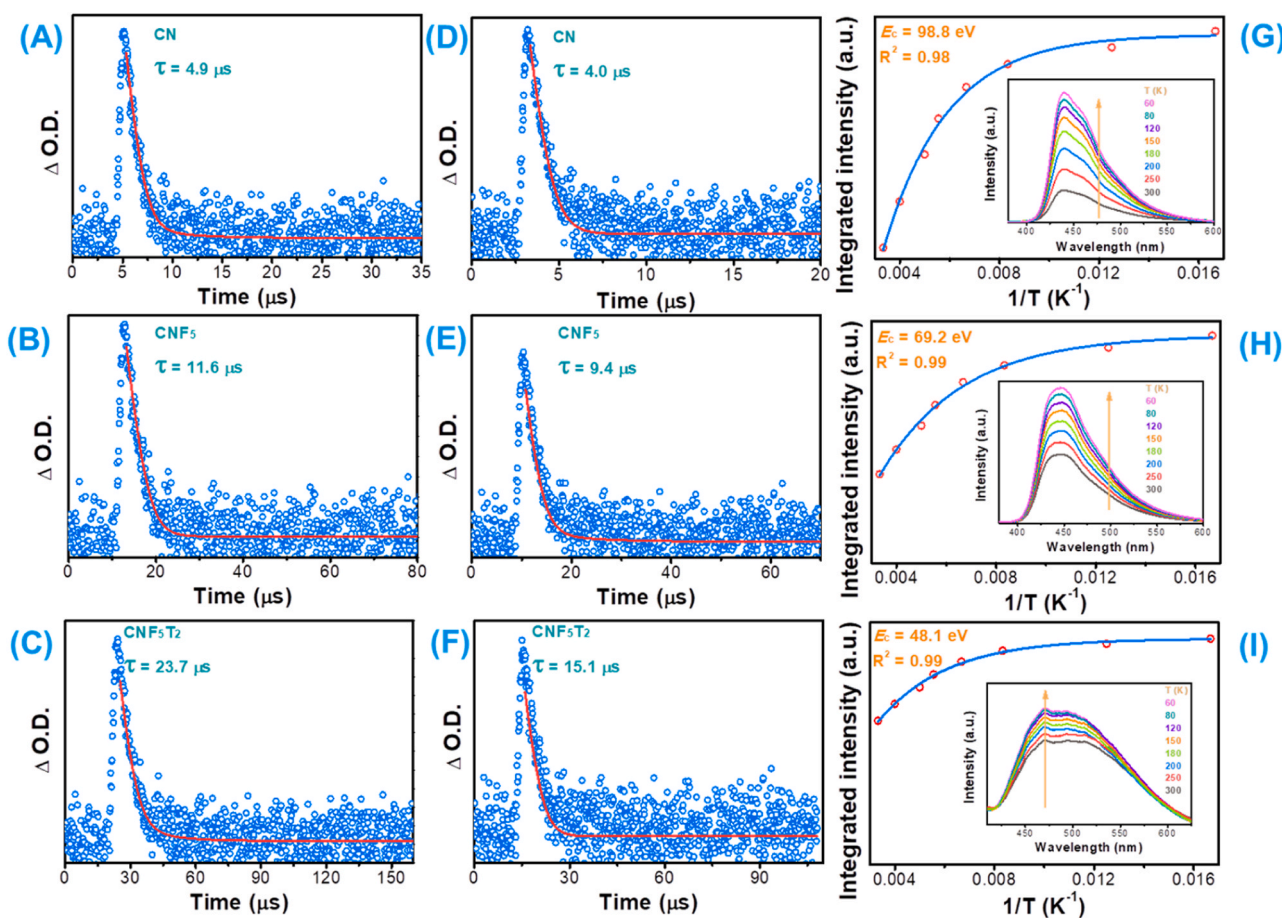

Fig. 4. The kinetics decay of CN, CNF_5, and CNF_5T_2 after pulsed excitation at 485 nm in transient absorption under Ar (A–C) and O_2 (D–F) at λ_{em} =450 nm, respectively. Integrated photoluminescence intensity as a function of the temperature of CN (G), CNF_5 (H), and CNF_5T_2 (I) and the corresponding temperature-dependent photoluminescence spectra (inset).

exciton binding energies (E_b) of the three samples were calculated to be 98.8 eV for CN, 69.2 eV for CNF$_5$, and 48.1 eV for CNF$_5$T$_2$ by employing the Arrhenius equation, respectively (Fig. 4G–I). For CNF$_5$T$_2$, its lowest E_b revealed that it could raise the dissociation of singlet excitons into free holes and electrons in the charge transfer process, and also effectively inhibit the dissipation of energy when singlet excitons were converted into triplet excitons, thus increasing the energy transfer ability [32]. Overall, it can be recognized that introducing Fe–N$_5$ and far Cv structures into the CN surface could simultaneously accelerate the efficiency of charge transfer and energy transfer in CN to improve the whole photocatalyst performance.

3.3. NO oxidation and universality

In recent years, photocatalytic removal of ppb–level of NO using a continuous flow reactor is an emerging attractive research area due to its mild reaction conditions and high efficiency, but it is still challenging under aerobic conditions because of the obstacle in the process of producing non–toxic by–products and the self-decomposition of the final products [12,41]. The reaction set up diagram for evaluating the performance of the photocatalysts is presented in Fig. S10. Typically, the photocatalytic NO oxidation over CN and CNF$_x$ proceeded sluggishly with a low conversion of 29.4% and 33.4–46.5%, respectively (Fig. 5A). CNF$_5$T$_2$ showed the best performance with 68.6% conversion of NO after 30 min (Fig. 5B). Surprisingly, the content of toxic NO$_2$ generated by CNF$_5$T$_y$ catalysts was expressively less than that of CN (61.5 ppb) and CNF$_x$ (37.2–52.8 ppb) in Fig. 5C and D. Especially, the representative CNF$_5$T$_2$ catalyst was only 3.9 ppb with a NO$_3^-$ selectivity of close to 100% (Fig. 5D), realizing the standard of zero discharge of pollutants to avoid the aerogel production that caused smog. Simultaneously, the content of NO$_3^-$ on the surface of CNF$_5$T$_2$ determined by ion chromatography was close to the theoretical amount (Fig. S11), further confirming that little NO$_2$ was formed. It was indicated that high coordination sites (Fe–N$_5$) and far Cv modification indeed gained unprecedented NO removal and NO$_3^-$ selectivity, significantly inhibiting the production of toxic intermediate NO$_2$. In addition, no strict change in NO conversion and NO$_2$ production over CNF$_5$T$_2$ was observed after the recycling test (Figs. 5E and S12), especially after exposing it to air for one month. No changes in the XRD peak of CNF$_5$T$_2$ were demonstrated before and after the reaction (Fig. 5F), clearly proving the satisfactory stability of CNF$_5$T$_2$.

Encouraged by the above–pronounced results, the developed photocatalyst synthetic method was further applied to a variety of precursors (cyanamide, dicyandiamide, thiourea, and urea) for the preparation of CN and other metal-organic complexes (dicarbonylcyclopentadienyl cobalt, cyclopentadienylmanganese tricarbonyl, and bis (cyclopentadienyl)dicarbonyl titanium). The color of these catalysts (Fig. 6A) was consistent with that of CNF$_5$T$_2$, and the deepening of the color, as the introduced high coordination number and far Cv structure on the CN surface, led to the expansion of the visible light absorption range. The two weak XRD peaks at 2θ of 13.0° and 27.3° were revealed for all the samples obtained by replacing different precursors (CA–Fe, DA–Fe, UR–Fe, and TU–Fe) and organometallic ligands (CN–Co, CN–Mn, and CN–Ti) (Fig. S13), which was similar to that of CNF$_5$T$_2$. In the meantime, these samples (CN–Co, CN–Mn, and CN–Ti) were also demonstrated to exhibit highly coordinated M–N$_5$ structures (Fig. S14 and Tables S3–S5). The NO removal rates of CA–Fe (60.0%), DA–Fe (61.1), UR–Fe (63.2%), and TU–Fe (65.8%) were higher than those of pure CA (26.0%), DA (28.6%), UR (32.4%), and TU (36.6%) (Fig. 6B). Similarly, the conversion rate of NO corresponding to CN–Co at 54.1%, CN–Mn at 62.4%, and CN–Ti at 66.4% was also markedly greater than that of CN at 29.4% (Fig. 6C). Among them (CA–Fe, DA–Fe, UR–Fe, TU–Fe, CN–Co, CN–Mn, and CN–Ti), the NO$_2$ generation was less than 10 ppb (Fig. 6D and E). Furthermore, under the same conditions, our optimized CNF$_5$T$_2$ catalyst exposed the best NO removal rate and NO$_3^-$ selectivity, compared with the reported catalysts (Fig. 6F) [9–11,42]. It was demonstrated that the synthesis strategies of these catalysts with excellent activity showed brilliant universality and had broad prospects in practical application.

3.4. Mechanism of NO removal

The mechanism of the selective oxidation of NO needs to be further inquired. In an anaerobic atmosphere, NO was hardly converted (Fig. S15), denoting that the NO oxidation was an aerobic process, and photogenerated e$^-$ and h$^+$ did not affect the performance. Therefore, it was reasonable to speculate that the activation of O$_2$ to produce highly oxidizing reactive oxygen species (ROSs) was critical. To elucidate the role of ROSs in photocatalytic NO oxidation, the quenching experiments of ROSs capture were explored by adding different scavenger agents. As we know, e$^-$, h$^+$, •OH, •O$_2^-$, ^{1}O$_2$, and H$_2$O$_2$ could be effectively trapped
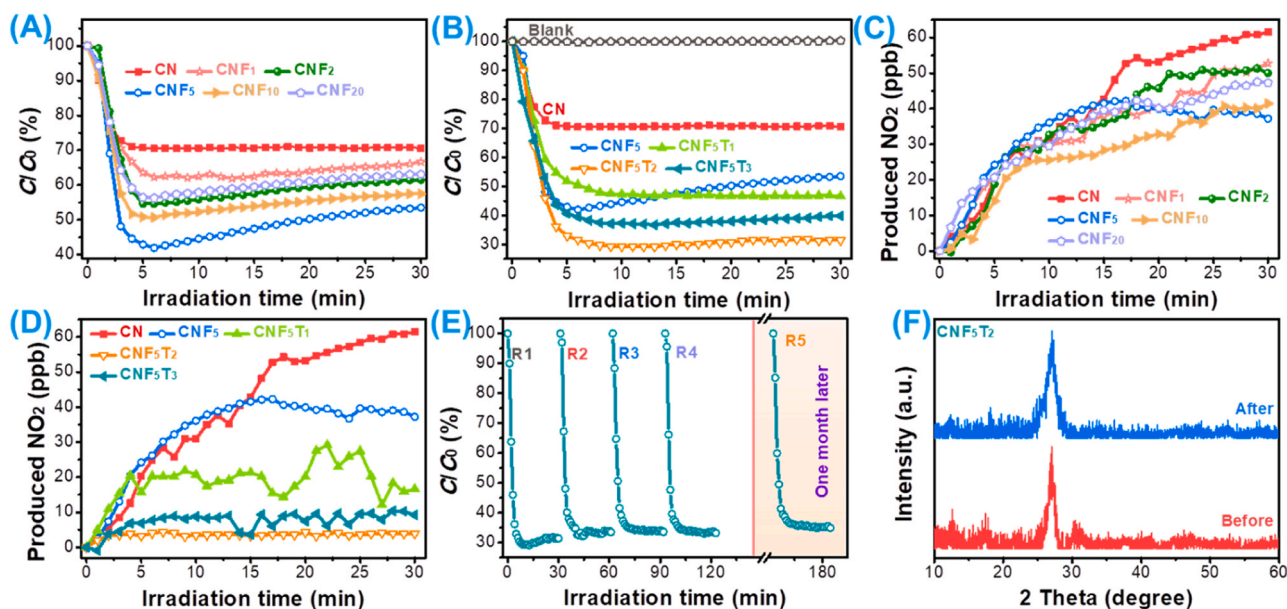

Fig. 5. Removal curves of NO (A and B) and generating curves for NO$_2$ (C and D) of *as*–prepared CN, CNF$_x$, and CNF$_5$T$_y$ samples. Recycling test of CNF$_5$T$_2$ (E). XRD patterns of CNF$_5$T$_2$ before and after photocatalytic test (F).
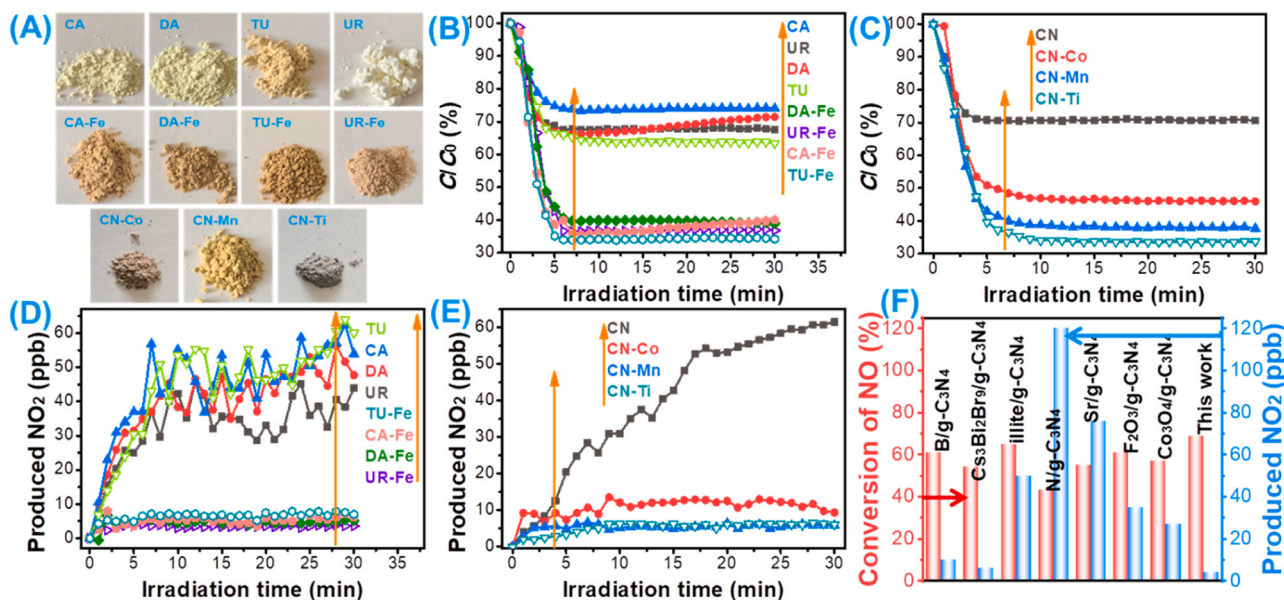
Fig. 6. The *as*–prepared samples images (A). Removal curves of NO (B and C), and generating curves for NO$_2$ (D and E) using other precursors and metals. Comparison of activity and NO$_3^-$ selectivity with other reported catalysts (F).

by K$_2$Cr$_2$O$_7$ (PD), K$_2$C$_2$O$_4$ (PO), *tert*-butyl alcohol (TBA), *p*-benzoquinone (PBQ), tryptophan (TR), and EDTA–Fe (FeE), respectively. As shown in Fig. 7A, after the addition of TR and PBQ, the photocatalytic NO removal efficiency was expressively reduced, indicating that $\bullet$O$_2^-$ and ^{1}O$_2$ were vital for NO removal over CNF$_5$T$_2$. However, the NO$_2$ generation was obviously accelerated after the introduction of TR, PBQ, and TBA in Fig. 7B, reflecting that the increase of NO$_3^-$ selectivity was related to $\bullet$O$_2^-$, ^{1}O$_2$, and $\bullet$OH for CNF$_5$T$_2$. Generally, the identification of the activation site of molecular O$_2$ contributed to distinguishing the origin of ROSs. *In situ* XPS indicated no evident changes in the binding energy of C 1 s peaks for CN, CNF$_5$, and CNF$_5$T$_2$ (Fig. S4B) under *in situ* illumination, but a positive shift of 0.4 eV on CN, 0.6 eV on CNF$_5$, and 0.2 eV on CNF$_5$T$_2$ for N 1 s peaks, and a negative shift of 0.7 eV over CNF$_5$ and 0.5 eV over CNF$_5$T$_2$ for Fe 2p peaks were observed after illumination (Fig. S4C and

D). In particular, the EPR intensity of these samples under dark was in the order of CN < CNF$_5$T$_2$ < CNF$_5$; in contrast, the trend of EPR intensity at irradiation was CN < CNF$_5$ < CNF$_5$T$_2$ (Fig. S5). In the charge difference distribution (Fig. 2E and F), the density of the blue electron cloud (blue and yellow electron clouds represent charge accumulation and consumption, respectively.) around the Fe–N sites and far–Cv in CNFN was also larger than that in CNF. These results indicated that the Fe–N$_5$ sites and far–Cv of CNF$_5$T$_2$ were able to accumulate photoexcited electrons, providing a site for charge transfer and energy transfer, thus activating O$_2$ to produce ROSs. Given this, we constructed the rational adsorption models to predict the activation of O$_2$. From the electron local function (*ELF*) in Fig. 7C–E, it was seen that the Fe atoms of CNF and CNFN and the adsorbed O$_2$ were endowed with electron cloud overlap, but the *ELF* value of O$_2$ of CNFN at 0.73 was smaller than that of
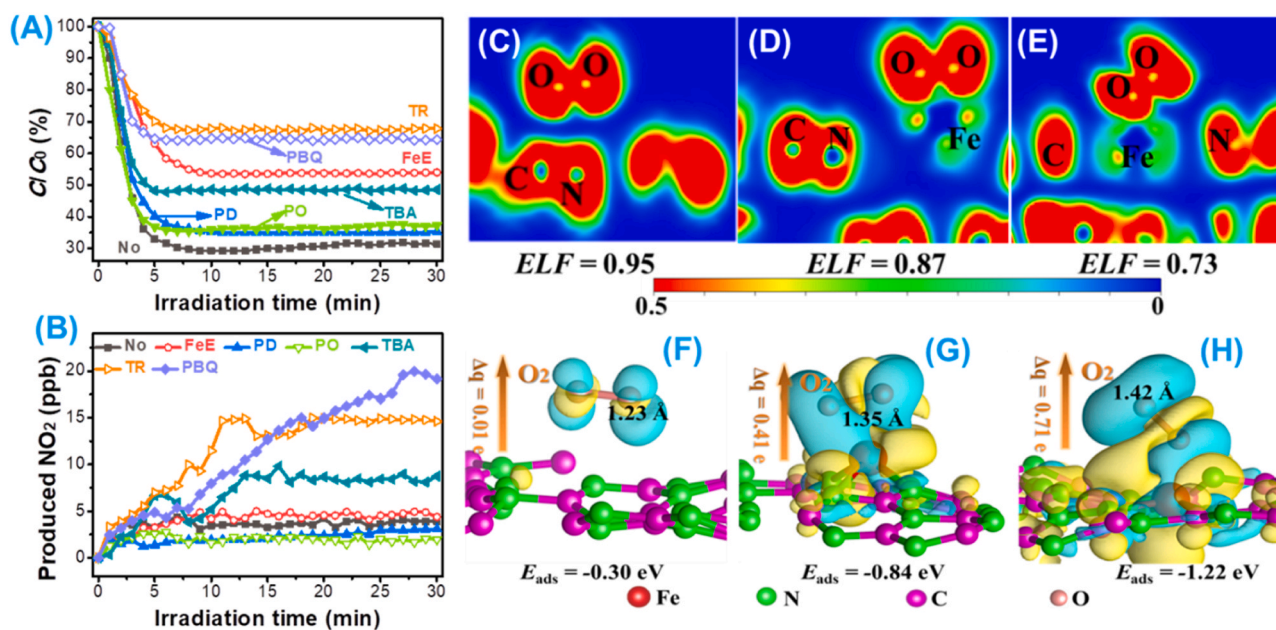

Fig. 7. Removal curves of NO (A) and generating curves for NO$_2$ (B) of CNF$_5$T$_2$ under the scavengers. The electron local function of adsorbed O$_2$ on CN (C), CNF (D), and CNFN (E). The charge difference distribution of adsorbed O$_2$ over CN (F), CNF (G), and CNFN (H).

CN at 0.95 and CNF at 0.87, insinuating O–O bond over CNFN with covalent weak interaction. Analogously, compared with CN (–0.30 eV) and CNF (–0.84 eV), the adsorption energy of O_2 (E_{ads}) was the largest for CNFN (–1.22 eV) in Fig. 4F–H. In comparison to CN (1.23 Å) and CNF (1.35 Å), the O–O bond was also the longest in CNFN (1.42 Å), and the Δq of O_2 increased from 0.01 e of CN to 0.41 e of CNF, and then to 0.71 e of CNFN (Fig. 7F–H). Importantly, the parallel structure of O_2 adsorption on the CNF surface became a vertical structure on the CNFN surface, which was advantageous to the energy transfer and charge transfer, facilitating the activation of O_2. *In situ* EPR was employed to monitor the effect of ROSs on the oxidation of NO in the presence of the trapping agents. As shown in Fig. 8A, upon irradiation, the DMPO–$\bullet O_2^-$ adducts intensity of CNF_5T_2 was greater than that of CN and CNF_5, directly validating that CNF_5T_2 was endowed with the fast charge transfer, producing the most photoexcited e^- to stimulate O_2, thereby forming more $\bullet O_2^-$. By contrast, the EPR intensity of the DMPO–$\bullet OH$ adducts of CNF_5T_2 was lower than that of CN and CNF_5 by photo–irradiation in Fig. 8B, reflecting the inaction of adsorbed H_2O for CNF_5T_2, in line with the FT–IR results (Fig. 1C). Alternatively, the theoretical calculation results also reflected that the modification of Fe–N_5 sites and Cv could significantly inhibit the adsorption and activation of H_2O (Fig. S16). As shown in Fig. S17A, the photocatalytic NO removal indicated a slight decrease with the increase of relative humidity (RH) from 5% to 80%. It might be attributed to the competitive adsorption of H_2O and NO. To our surprise, the formation of NO_2 improved from 3.9 ppb at RH = 5% to 16.4 ppb at RH = 40%, and then decreased to 1.2 ppb at RH = 80% (Fig. S17B). It was illustrated that RH did not affect the NO conversion, and the increase of RH also activated H_2O to rapidly form NO_2. However, excess RH promoted the reaction of NO_2 with H_2O, leading to a decrease in generating NO_2. As a result, the

weakening of H_2O adsorption and activation could be considered an effective strategy to accurately regulate NO_3^- selectivity. Again, after illumination, the TEMP–$^1O_2$ adducts intensity of CNF_5T_2 was broadly higher than that of CN and CNF_5 (Fig. 8C), which accelerated the energy transfer to activate O_2, ulteriorly leading to more $^1O_2$ generation. In general, $^1O_2$ generation could be dedicated to the energy transfer process and the firsthand reaction of $\bullet O_2^-$ and photoexcited h^+ [12]. Therefore, after the addition of PO trapping h^+, the EPR signal of $^1O_2$ corresponding to CN and CNF_5 rapidly decreased, whereas CNF_5T_2 was almost unchanged (Fig. 8C), further authenticating that CNF_5T_2 enabled the $^1O_2$ formation by energy transfer, rather than by the reaction between $\bullet O_2^-$ and h^+. In this context, the embellishment of the Fe–N_5 structures with high coordination number and far Cv could improve the charge transfer and energy transfer of excitons in CN to form abundant $\bullet O_2^-$ and $^1O_2$, respectively, and inhibit the activation of H_2O to generate $\bullet OH$. Therefore, CNF_5T_2 was blessed with a superior NO removal rate and admirable NO_3^- selectivity.

Tracing the intermediates of photocatalytic NO oxidation was very convenient for analyzing the mechanism of the excellent performance by *in situ* diffuse reflectance FT–IR (*in situ* DRIFTS). Notably, all the FT–IR peaks corresponding to the intermediates were recorded in Table S3. During adsorption and illumination, the undissociated H_2O peak at 1904 and 1630 cm^{-1} of CNF_5T_2 was expressively lower than that of CN and CNF_5 (Fig. 8D–F), meaning the inhibited adsorption and activation of H_2O, which is similar to the results of FT–IR (Fig. 1C) and EPR (Fig. 8B). The absorbance at 1160 cm^{-1} (N–OH) aggrandized over time under adsorption or illumination for CN. Conversely, N–OH was only seen in the adsorption of CNF_5, and even more, it was not found in CNF_5T_2. Upon irradiation (Fig. 8H), adsorbed NO_2 at 1322 cm^{-1} only existed in CNF_5. Similarly, the asymmetric stretching vibration of NO_2 ($\nu_{asym}.NO_2$)
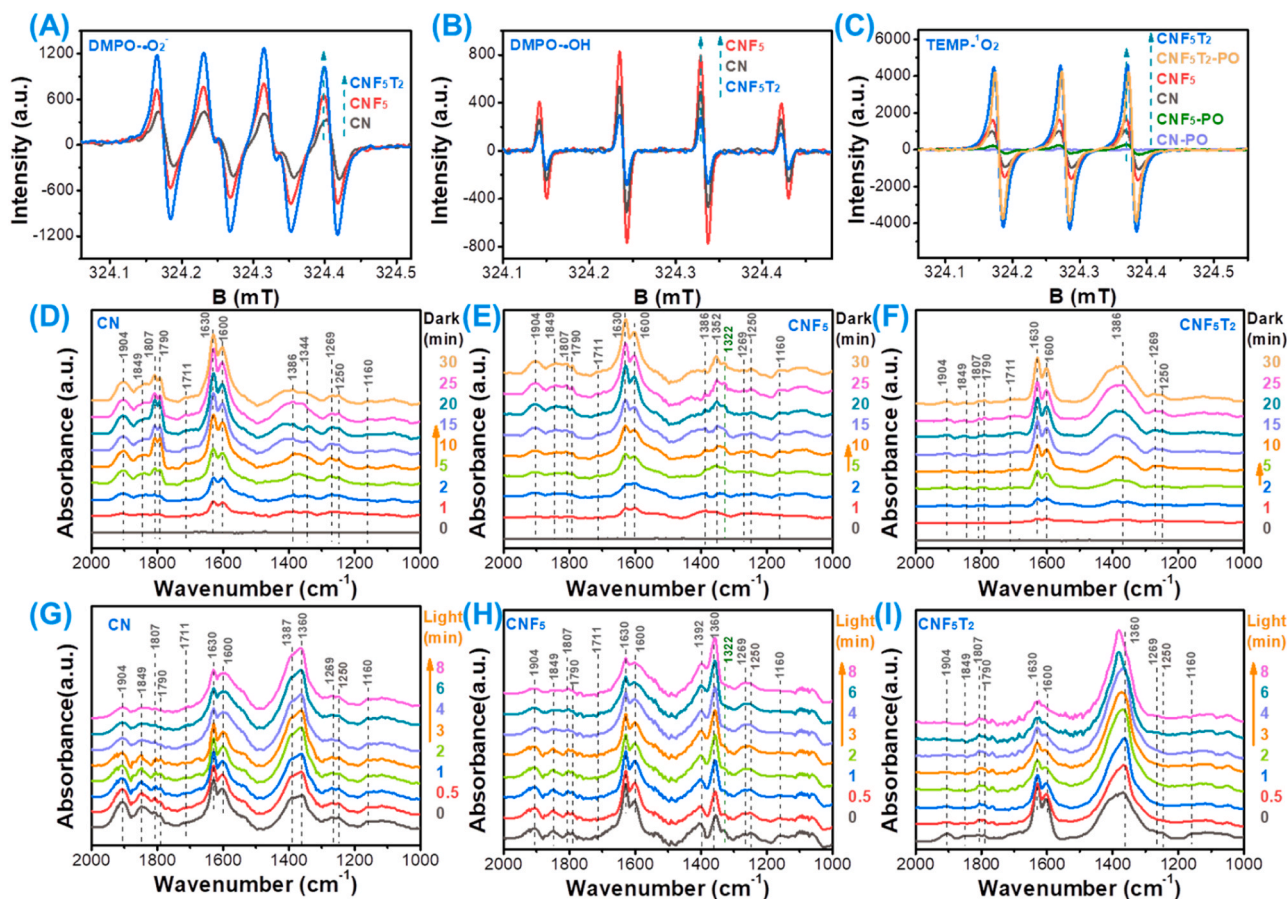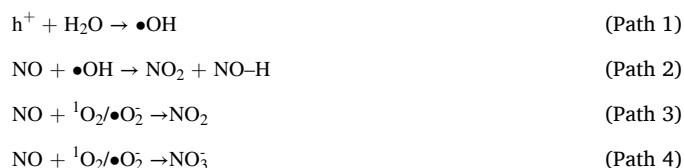

Fig. 8. ESR adducts signals of captured $\bullet O_2^-$ (A), $\bullet OH$ (B) and $^1O_2$ (C) under illumination. *In situ* DRIFTS during adsorption and reactivity over CN (D and G), CNF_5 (E and H), and CNF_5T_2 (F and I).

at 1600 cm^{-1} and symmetric stretching vibration of NO$_2$ ($\nu_{sym.}$NO$_2$) at 1386 cm^{-1} were slowly consumed in CN and CNF$_5$ with the increased illumination (Fig. 8G and H). Surprisingly, there were no intermediates ($\nu_{asym.}$NO$_2$ and $\nu_{sym.}$NO$_2$) on CNF$_5$T$_2$ (Fig. 8I). Based on these considerations, in contrast to CN and CNF$_5$, this conjectural process (Path 1, Path 2, and Path 3) was blocked in CNF$_5$T$_2$ to confine the generation of NO$_2$, gaining the superior NO$_3^-$ selectivity [23]. In adsorption, these peaks at 1849 (NO), 1807 (linear NO), 1790 (νNO), 1711 (adsorbed HNO$_2$), 1600 ($\nu_{asym.}$ NO$_2$), 1386 ($\nu_{sym.}$NO$_2$), 1269 (NO$_2^-$), and 1250 cm^{-1} (bridging NO$_3^-$) over CN, CNF$_5$ and CNF$_5$T$_2$ gradually increased with the evolution of time (Fig. 8D–F), suggesting that weak oxidation of NO was initiated during adsorption. In contrast, these peaks relaxedly weakened with the evolution during irradiation, while the intensity of free NO$_3^-$ corresponding to 1358 cm^{-1} was tardily enhanced on the surface of these three samples (Fig. 8G–8I), especially in CNF$_5$T$_2$ was the strongest. It was indicated that CNF$_5$T$_2$ was more able to promote the rate of Path 4 than CN and CNF$_5$, and therefore, CNF$_5$T$_2$ exhibited superior NO conversion rate and NO$_3^-$ selectivity.

$$h^+ + H_2O \rightarrow \bullet OH \qquad \text{(Path 1)}$$

$$NO + \bullet OH \rightarrow NO_2 + NO\text{–}H \qquad \text{(Path 2)}$$

$$NO + {}^1O_2/\bullet O_2^- \rightarrow NO_2 \qquad \text{(Path 3)}$$

$$NO + {}^1O_2/\bullet O_2^- \rightarrow NO_3^- \qquad \text{(Path 4)}$$

From a theoretical calculation perspective, the relative energy for the formed toxic intermediate NO$_2$ decreased from –0.71 eV over CNFN to –0.96 eV over CNF and then to –1.08 eV over CN (Fig. 9A), while the relative energy of generation of NO$_3^-$ enhanced from –2.66 eV for CNFN to –1.58 eV for CNF and then to –1.20 eV for CN (Fig. 9B). These results ascertained the fact that pure CN and modified CN with a low coordination number (Fe–N$_4$ sites) were more favorable to the formation of toxic intermediate NO$_2$ in thermodynamics. In contrast, the modified CN with highly coordinated structure (Fe–N$_5$ sites) and far Cv tended to convert NO into NO$_3^-$ instead of NO$_2$.

Besides, the adsorption of NO molecule and specific surface area, as an important factor affecting the photocatalytic performance, also needs to be demonstrated. In the electron local function (*ELF*) from Fig. 9C–E, the electron clouds overlapped between Fe atoms and adsorbed NO molecules. However, the *ELF* value of NO on CNFN (0.70) was less than 0.82 on CN and 0.76 on CNF at 0.93, implying that the covalent interaction of N–O bonds in CNFN was seriously weakened. Equally, CNFN (–1.64 eV) showed the largest adsorption energy (*E*$_{ads}$) for NO compared to CN (–0.19 eV) and CNF (–1.06 eV) in Fig. 9F–H. Compared with CN (1.16 Å) and CNF (1.19 Å), the O–N bond of CNFN was also the longest (1.24 Å). The Δq of NO increased from 0.09 e over CN to 0.35 e over CNF, and then to 1.21 e over CNFN (Fig. 9F–H). Most importantly, the vertical structure of NO adsorption only existed on CNFN surface, which was profitable to the adsorption and activation of NO, so as to enhance the NO conversion. The physical properties of CN, CNF$_5$, and CNF$_5$T$_2$
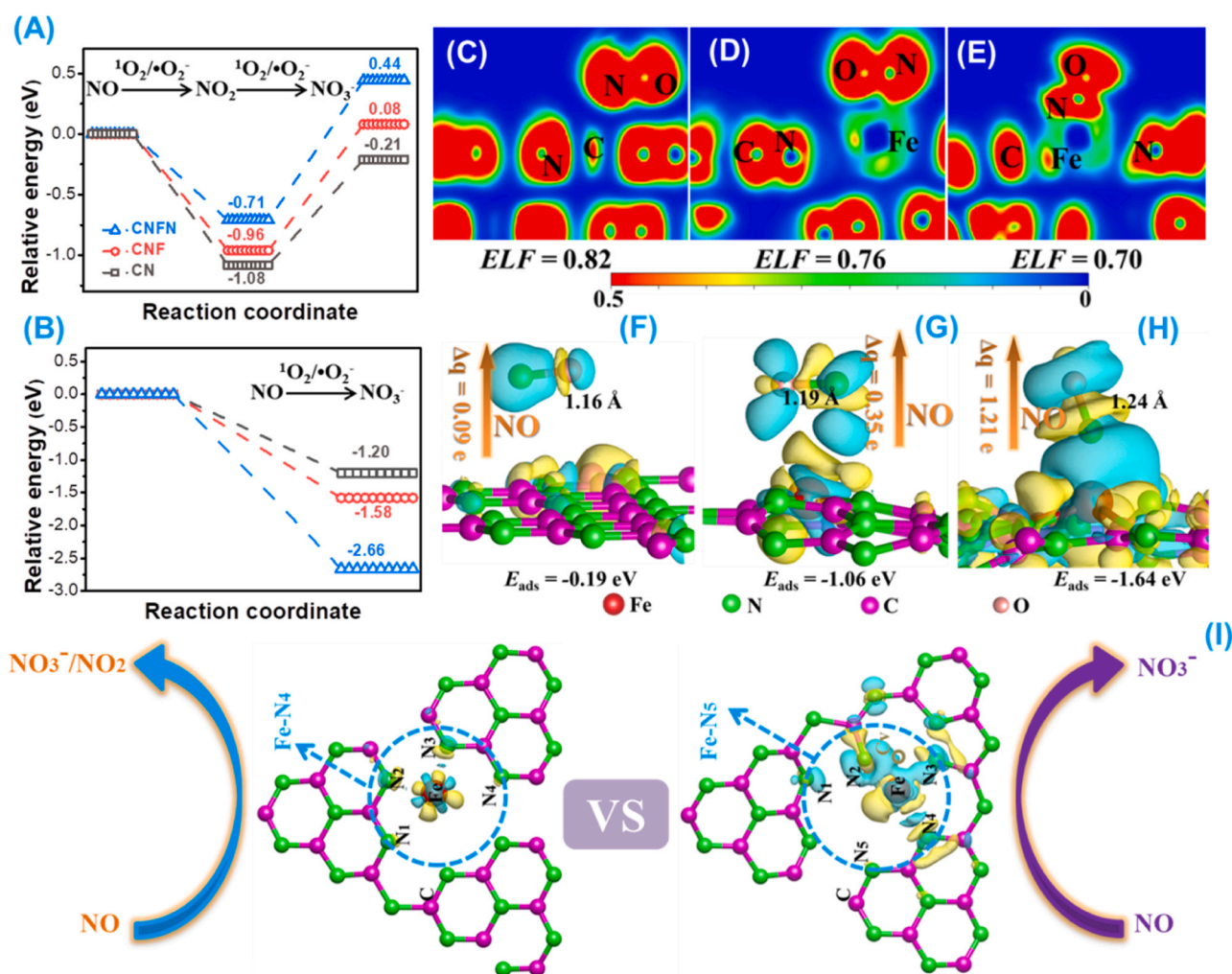

Fig. 9. The calculated reaction pathways for NO oxidation (A and B). Electron local function (C–E) and charge difference distribution (F–H) of adsorbed NO on CN, CNF, and CNFN, respectively. Comparison of the NO removal mechanism between CNF$_5$ and CNF$_5$T$_2$ (I).

obtained by the nitrogen sorption isotherms (Fig. S18A) and corresponding pore size distribution curves (Fig. S18B) were listed in Table S7. The corresponding NO removal rate per unit surface area of CN, CNF_5, and CNF_5T_2 were calculated to be 0.026, 0.039, and 0.033 (Fig. S19), respectively, clearly illustrating that the surface area did not affect the photocatalyst activity.

According to the linear intersection approach [43], the flat band potentials were calculated to be –0.50 V on CN, –0.59 V on CNF_5, and –0.42 V on CNF_5T_2 (vs Ag/AgCl) using the X-intercept in the Mott Schottky plots (Fig. S20A–C), respectively. Then the CB potential (vs NHE) was obtained to be –0.77 V on CN, –0.86 V on CNF_5, and –0.69 V on CNF_5T_2 (vs NHE) by the reference electrode potential transformation, respectively [17]. The band gap energies (E_g) of CN, CNF_5, and CNF_5T_2 were measured as 2.74 eV, 2.62 eV, and 1.85 eV (Fig. S20D), respectively. Thus, the valence band (VB) potential of CN, CNF_5, and CNF_5T_2 were procured to be +1.97 V, +1.76 V, and +1.16 V with the equation VB (vs NHE) = CB (vs NHE) + E_g, respectively (Fig. S21). According to the reports, the $O_2/•O_2^-$ redox potential could thermodynamically activate the O_2 molecular [44]. As outlined above, a possible mechanism of NO oxidation was proposed and shown in Fig. 9I. In contrast to the modification of the structure with a low coordination number ($Fe–N_4$), the introduction of the higher coordination number structure ($Fe–N_5$) and far–Cv could not only improve the energy transfer and charge transfer process of exciton in CN, promoting the adsorption and activation of O_2 to enhance the generation of $•O_2^-$ and $^1O_2$, but also inhibit the dissociation of H_2O to produce $•OH$, both of which contributed to increasing the removal rate of NO and NO_3 selectivity.

4. Conclusion

In summary, this work provides an attractive strategy for reconstructing the highly coordinated structure to improve the photocatalyst efficiency and selectivity in the oxidative conversion of NO in ultra–low concentrations to exclusively give NO_3 using green and inexpensive photocatalytic techniques, significantly inhibiting the formation of environment–hazardous by–product NO_2. The precise construction of active sites with high coordination numbers and far defects by a simple roasting method could not only promote the energy and charge transfer in the activating O_2 process to generate $•O_2^-$ and $^1O_2$, but also inhibit the generation of $•OH$ because of weak activation of adsorbed H_2O. The oriented formation of $•O_2^-$ and $^1O_2$, without $•OH$, was involved in the NO removal to achieve deep oxidation and synchronously limit the NO_2 formation. This work reveals the relationship between the precise regulation of the coordination environment of the active sites and the directional generation of specific ROSs, and also inspires new ideas for the rational design of superior photocatalysts to be applied in a variety of environmental remediation fields.

CRediT authorship contribution statement

Yujiao Zhang: Writing – original draft, Methodology, Investigation, Formal analysis, Data curation, Conceptualization. **Zhao Hu:** Writing – review & editing, Writing – original draft, Resources, Project administration, Methodology, Investigation, Formal analysis, Data curation, Conceptualization. **Yan Wang:** Investigation, Formal analysis, Data curation, Conceptualization. **Jinshu Huang:** Visualization, Validation, Supervision, Data curation. **Song Yang:** Writing – review & editing, Visualization, Validation, Funding acquisition, Data curation, Conceptualization. **Hu Li:** Writing – review & editing, Writing – original draft, Supervision, Software, Resources, Project administration, Methodology, Investigation, Funding acquisition, Formal analysis, Data curation, Conceptualization.

Declaration of Competing Interest

The authors declare that they have no known competing financial interests or personal relationships that could have appeared to influence the work reported in this paper.

Data availability

Data will be made available on request.

Appendix A. Supporting information

Supplementary data associated with this article can be found in the online version at doi:10.1016/j.apcatb.2024.123948.

References

[1] J. Li, X.Y. Liu, H. Wong, Y.J. Sun, F. Dong, Prediction and interpretation of photocatalytic NO removal on g-C_3N_4-based catalysts using machine learning, Chin. Chem. Lett. 35 (2024) 108596.

[2] R.M. Chen, J.Y. Li, J.L. Wang, W.P. Yang, S.J. Shen, F. Dong, Continuous NO upcycling into ammonia promoted by SO_2 in flue gas: poison can be a gift, Environ. Sci. Technol. 57 (2023) 12127–12134.

[3] M. Marchi, E. Raciti, S.M. Gali, F. Piccirilli, H. Vondracek, A. Actis, E. Salvadori, C. Rosso, A. Criado, C. D'Agostino, L. Forster, D. Lee, A.C. Foucher, R.K. Rai, D. Beljonne, E.A. Stach, M. Chiesa, R. Lazzaroni, G. Filippini, M. Prato, M. Melchionna, P. Fornasiero, Carbon vacancies steer the activity in dual Ni carbon nitride photocatalysis, Adv. Sci. 10 (2023) 202303781.

[4] D.M. Zhao, Y.Q. Wang, C.L. Dong, Y.C. Huang, J. Chen, F. Xue, S.H. Shen, L.J. Guo, Boron-doped nitrogen-deficient carbon nitride-based Z-scheme heterostructures for photocatalytic overall water splitting, Nat. Energy 6 (2021) 388–397.

[5] R.C. Cao, M.Q. Zhang, C.Q. Hu, D.Q. Xiao, M. Wang, D. Ma, Catalytic oxidation of polystyrene to aromatic oxygenates over a graphitic carbon nitride catalyst, Nat. Commun. 13 (2022) 4809.

[6] S. Xu, P. Zhou, Z. Zhang, C. Yang, B. Zhang, K. Deng, S. Bottle, H. Zhu, Selective oxidation of 5-hydroxymethylfurfural to 2,5-furandicarboxylic acid Using O_2 and a photocatalyst of co-thioporphyrazine bonded to g-C_3N_4, J. Am. Chem. Soc. 139 (2017) 14775–14782.

[7] X. Xiao, Y. Gao, L. Zhang, J. Zhang, Q. Zhang, Q. Li, H. Bao, J. Zhou, S. Miao, N. Chen, J. Wang, B. Jiang, C. Tian, H. Fu, A promoted charge separation/transfer system from Cu single atoms and C_3N_4 layers for efficient photocatalysis, Adv. Mater. (2020) 2003082.

[8] L.X. Wang, B.C. Zhu, J.J. Zhang, J.B. Ghasemi, M. Mousavi, J.G. Yu, S-scheme heterojunction photocatalysts for CO_2 reduction, Matter (2022) 4187–4211.

[9] B.K. Xie, D.Y. Chen, N.J. Li, Q.F. Xu, H. Li, J.M. Lu, Lead-free $Cs_3Bi_2Br_9$ perovskite In-situ growth on 3D flower-like g-C_3N_4 microspheres to improve photocatalytic performance, Chem. Eng. J. 452 (2023) 139662.

[10] M. Zhou, G.H. Dong, F.K. Yu, Y. Huang, The deep oxidation of NO was realized by Sr multi-site doped g-C_3N_4 via photocatalytic method, Appl. Catal. B 256 (2019) 117825.

[11] X. Li, G.H. Dong, F.G. Guo, P.F. Zhu, Y. Huang, C.Y. Wang, Enhancement of photocatalytic NO removal activity of g-C_3N_4 by modification with illite particles, Environ. Sci. Nano 7 (2020) 1990–1998.

[12] S.X. Wang, W. Cui, B. Lei, X.A. Dong, Y. Tang, F. Dong, Targeted NO oxidation and synchronous NO_2 inhibition via oriented $^1O_2$ formation based on lewis acid site adjustment, Environ. Sci. Technol. 57 (2023) 12890–12900.

[13] B.G. Wu, L.P. Zhang, B.J. Jiang, Q. Li, C.G. Tian, Y. Xie, W.Z. Li, H.G. Fu, Ultrathin porous carbon nitride bundles with an adjustable energy band structure toward simultaneous solar photocatalytic water splitting and selective phenylcarbinol oxidation, Angew. Chem. Int. Ed. 60 (2021) 4815–4822.

[14] A. Wang, J. Li, T. Zhang, Heterogeneous single-atom catalysis, Nat. Rev. Chem. 2 (2018) 65–81.

[15] T. Yang, X.N. Mao, Y. Zhang, X.P. Wu, L. Wang, M.Y. Chu, C.W. Pao, S.Z. Yang, Y. Xu, X.Q. Huang, Coordination tailoring of Cu single sites on C_3N_4 realizes selective CO_2 hydrogenation at low temperature, Nat. Commun. 12 (2021) 6022.

[16] B.H. Lee, S. Park, M. Kim, A.K. Sinha, S.C. Lee, E. Jung, W.J. Chang, K.S. Lee, J. H. Kim, S.P. Cho, H. Kim, K.T. Nam, T. Hyeon, Reversible and cooperative photoactivation of single-atom Cu/TiO_2 photocatalysts, Nat. Mater. 18 (2019) 620–626.

[17] Z. Hu, Y.J. Zhang, L. Pu, B.Y. Wang, S. Yang, H. Li, Atomic Ti-Nx sites with switchable coordination number for enhanced visible-light photocatalytic water disinfection, J. Clean. Prod. 377 (2022) 134423.

[18] T. Wang, X.Q. Tao, X.L. Li, K. Zhang, S.J. Liu, B.X. Li, Synergistic Pd single atoms, clusters, and oxygen vacancies on TiO_2 for photocatalytic hydrogen evolution coupled with selective organic oxidation, Small 17 (2021) 2006255.

[19] G.Y. Feng, H. Huang, M. Zhang, Z.L. Wu, D.D. Sun, Q.Q. Chen, D.Y. Yang, Y. Y. Zheng, Y. Chen, X.X. Jing, Single atom iron-doped graphic-Phase C_3N_4 semiconductor nanosheets for augmented sonodynamic melanoma therapy synergy with endowed chemodynamic effect, Adv. Sci. 10 (2023) e2302579.

[20] L.S. Zhang, X.H. Jiang, Z.A. Zhong, L. Tian, Q. Sun, Y.T. Cui, X. Lu, J.P. Zou, S. L. Luo, Carbon nitride supported high-loading Fe single-atom catalyst for activation of peroxymonosulfate to generate $^1O_2$ with 100% selectivity, Angew. Chem. Int. Ed. 60 (2021) 21751–21755.

[21] S.J. Wei, Y.B. Sun, Y.Z. Qiu, A. Li, C.Y. Chiang, H. Xiao, J.S. Qian, Y.D. Li, Self-carbon-thermal-reduction strategy for boosting the Fenton-like activity of single Fe-N_4 sites by carbon-defect engineering, Nat. Commun. 14 (2023) 7549.

[22] Y. He, J.P. Sheng, Q. Ren, Y.J. Sun, W.C. Hao, F. Dong, Operando identification of dynamic photoexcited oxygen vacancies as true catalytic active sites, ACS Catal. 13 (2023) 2191–2203.

[23] Y.J. Zhang, Z. Hu, H. Zhang, H. Li, S. Yang, Uncovering original Z scheme heterojunctions of COF/MOx (M = Ti, Zn, Zr, Sn, Ce, and Nb) with ascendant photocatalytic selectivity for virtually 99.9% NO-to-NO_3^- oxidation, Adv. Funct. Mater. (2023) 2303851.

[24] Q.H. Liang, Z. Li, Z.H. Huang, F.Y. Kang, Q.H. Yang, Holey graphitic carbon nitride nanosheets with carbon vacancies for highly improved photocatalytic hydrogen production, Adv. Funct. Mater. 25 (2015) 6885–6892.

[25] H. Shang, M. Li, H. Li, S. Huang, C. Mao, Z. Ai, L. Zhang, Oxygen vacancies promoted the selective photocatalytic removal of NO with blue TiO_2 via simultaneous molecular oxygen activation and photogenerated hole annihilation, Environ. Sci. Technol. 53 (2019) 6444–6453.

[26] L.Y. Zhu, H. Zhong, D. Du, T. Li, H. Nguyen, S.P. Beckman, W.T. Xu, J.C. Li, N. Cheng, Y.H. Lin, A peroxidase-like single-atom Fe-N_5 active site for effective killing human lung adenocarcinoma cells, Nano Res. 16 (2022) 5216–5225.

[27] H. Tan, P. Zhou, M.X. Liu, Q.H. Zhang, F.Y. Liu, H.Y. Guo, Y. Zhou, Y. Chen, L. Y. Zeng, L. Gu, Z.F. Zheng, M.Q. Tong, S.J. Guo, Photocatalysis of water into hydrogen peroxide over an atomic Ga-N_5 site, Nat. Synth. 2 (2023) 557–563.

[28] P.G. Tratnyek, M.S. Elovitz, P. Colverson, Photoeffects of textile dye wastewaters: sensitization of singlet oxygen formation, oxidation of phenols and toxicity to bacteria, Environ. Toxicol. Chem. 13 (1994) 27–33.

[29] Y. Nosaka, A.Y. Nosaka, Generation and detection of reactive oxygen species in photocatalysis, Chem. Rev. 117 (2017) 11302–11336.

[30] R. Hailili, H.W. Ji, K.W. Wang, X.A. Dong, C.C. Chen, H. Sheng, D.W. Bahnemann, J.C. Zhao, ZnO with controllable oxygen vacancies for photocatalytic nitrogen oxide removal, ACS Catal. 12 (2022) 10004–10017.

[31] B. Han, Y.L. Guo, Y.K. Huang, W. Xi, J. Xu, J. Luo, H.F. Qi, Y.J. Ren, X.Y. Liu, B. T. Qiao, T. Zhang, Strong metal-support interactions between Pt single atoms and TiO_2, Angew. Chem. Int. Ed. 59 (2020) 11824–11829.

[32] G.Q. Zhang, Y.S. Xu, M. Rauf, J.Y. Zhu, Y.L. Li, C.X. He, X.Z. Ren, P.X. Zhang, H. W. Mi, Breaking the limitation of elevated coulomb interaction in crystalline carbon nitride for visible and near-infrared light photoactivity, Adv. Sci. (2022) 2201677.

[33] H. Yu, R. Shi, Y. Zhao, T. Bian, Y. Zhao, C. Zhou, G.I.N. Waterhouse, L.Z. Wu, C. H. Tung, T. Zhang, Alkali-assisted synthesis of nitrogen deficient graphitic carbon nitride with tunable band structures for efficient visible-light-driven hydrogen evolution, Adv. Mater. 29 (2017) 1605148–1605155.

[34] S.F. An, G.H. Zhang, T.W. Wang, W.N. Zhang, K.Y. Li, C.S. Song, J.T. Miller, S. Miao, J.H. Wang, X.W. Guo, High-density ultra-small clusters and single-atom Fe sites embedded in graphitic carbon nitride g-C_3N_4 for highly efficient catalytic advanced oxidation processes, ACS Nano 12 (2018) 9441–9450.

[35] D.C. Jiang, S.N. Hu, Y. Qu, X. Tian, H.W. Du, C.H. Zhu, Z.J. Li, L.S. Yin, Y.P. Yuan, G. Liu, Infrared irradiation-lattice vibration coupling-initiated N→N* electronic transition in carbon nitride nanosheets for increased photocatalysis, Adv. Funct. Mater. (2024) 2311803.

[36] D.B. Lobell, S.D. Tommaso, J.A. Burney, Globally ubiquitous negative effects of nitrogen dioxide on crop growth, Sci. Adv. 8 (2022) eabm9909.

[37] M. Ozkan, K.A.M. Quiros, J.M. Watkins, T.M. Nelson, N.D. Singh, M. Chowdhury, T. Namboodiri, K.R. Talluri, E. Yuan, Curbing pollutant CO_2 by using two-dimensional MXenes and MBenes, Chem 10 (2023) 1–41.

[38] Y.Y. Qian, D.D. Li, Y.L. Han, H.L. Jiang, Photocatalytic molecular oxygen activation by regulating excitonic effects in covalent organic frameworks, J. Am. Chem. Soc. 142 (2020) 20763–20771.

[39] A. Actis, M. Melchionna, G. Filippini, P. Fornasiero, M. Prato, M. Chiesa, E. Salvadori, Singlet-triplet energy Inversion in carbon nitride photocatalysts, Angew. Chem. Int. Ed. 62 (2023) 202313540.

[40] Y.Z. Peng, G.C. Guo, S. Guo, L.H. Kong, T.B. Lu, Z.M. Zhang, Charge transfer from donor to acceptor in conjugated microporous polymer for enhanced photosensitization, Angew. Chem. Int. Ed. 60 (2021) 22062–22069.

[41] S.H. Xie, W. Tan, Y.J. Li, L. Ma, S.N. Ehrlich, J.G. Deng, P. Xu, F. Gao, L. Dong, F. D. Liu, Copper single atom-triggered niobia–ceria catalyst for efficient low-temperature reduction of nitrogen oxides, ACS Catal. 12 (2022) 2441–2453.

[42] X. Xia, C. Xie, Q.D. Che, P. Yang, Potassium-derived charge channels in boron-Doped g-C_3N_4 nanosheets for photocatalytic NO oxidation and hydrogen evolution, Langmuir 39 (2023) 1250–1261.

[43] C.Y. Feng, L. Tang, Y.C. Deng, J.J. Wang, J. Luo, Y.N. Liu, X.L. Ouyang, H.R. Yang, J.F. Yu, J.J. Wang, Synthesis of leaf-vein-like g-C_3N_4 with tunable band structures and charge transfer properties for selective photocatalytic H_2O_2 evolution, Adv. Funct. Mater. 30 (2020) 2001922.

[44] L. Yang, B.S. Tian, Y. Xie, S.M. Dong, M.Q. Yang, S.L. Gai, J. Lin, Oxygen-vacancy-rich piezoelectric BiO_{2-x} nanosheets for augmented piezocatalytic, sonothermal, and enzymatic therapies, Adv. Mater. 35 (2023) 2300648.